Swansea University
Prifysgol Abertawe

Cronfa
Setting Research Free

Swansea University E-Theses

Corrosion mechanisms and corrosion inhibition of commercial purity magnesium and advanced magnesium alloys.

Grace, Richard William

How to cite:

Grace, Richard William (2012) *Corrosion mechanisms and corrosion inhibition of commercial purity magnesium and advanced magnesium alloys..* thesis, Swansea University.
http://cronfa.swan.ac.uk/Record/cronfa43082

Use policy:

This item is brought to you by Swansea University. Any person downloading material is agreeing to abide by the terms of the repository licence: copies of full text items may be used or reproduced in any format or medium, without prior permission for personal research or study, educational or non-commercial purposes only. The copyright for any work remains with the original author unless otherwise specified. The full-text must not be sold in any format or medium without the formal permission of the copyright holder. Permission for multiple reproductions should be obtained from the original author.

Authors are personally responsible for adhering to copyright and publisher restrictions when uploading content to the repository.

Please link to the metadata record in the Swansea University repository, Cronfa (link given in the citation reference above.)

http://www.swansea.ac.uk/library/researchsupport/ris-support/

Prifysgol Abertawe
Swansea University

Corrosion Mechanisms and Corrosion Inhibition of Commercial Purity Magnesium and Advanced Magnesium Alloys

Richard William Grace

Supervisor:
Dr. Geraint Williams,
College of Engineering,
Swansea University

Submitted to the University of Wales in fulfilment of the requirements for the
Degree of Doctor of Philosophy,
Swansea University,
October, 2012.

SWANSEA UNIVERSITY LIBRARY

ProQuest Number: 10821474

All rights reserved

INFORMATION TO ALL USERS
The quality of this reproduction is dependent upon the quality of the copy submitted.

In the unlikely event that the author did not send a complete manuscript
and there are missing pages, these will be noted. Also, if material had to be removed,
a note will indicate the deletion.

ProQuest 10821474

Published by ProQuest LLC (2018). Copyright of the Dissertation is held by the Author.

All rights reserved.
This work is protected against unauthorized copying under Title 17, United States Code
Microform Edition © ProQuest LLC.

ProQuest LLC.
789 East Eisenhower Parkway
P.O. Box 1346
Ann Arbor, MI 48106 – 1346

“*Perfer et obdura, dolor hic tibi proderit olim.*”

--Ovid

This thesis is dedicated to the memory of my father, Terence Grace, who passed away before its submission. It was the example of his hard work, ingenuity, and continually enquiring mind that led me to science, and ultimately to the completion of my doctoral work.

ABSTRACT

Magnesium is a metal with many desirable engineering properties with the most commercially attractive being its excellent strength to weight ratio, making it the lightest structural metal used today. Despite Magnesium's many advantages, its major limitation which has hindered its uses in applications across the engineering spectrum is its poor corrosion resistance. This is in part due to a lack of understanding of the corrosion mechanisms that occur on both Commercial purity (C.P.) magnesium and advance magnesium alloys. It is the objective of this thesis to spread some light on the fundamental corrosion mechanisms behind the aggressive nature of the metals corrosion and also corrosion prevention through the use of inhibitor coatings.

This body of work is two fold. Firstly, it deals with the effects of chloride induced filiform of organic coated magnesium in which a new proposed mechanism for the advancement of filiform propagation is given. Contradictory to current literature, it is proposed that filiform propagation is caused by"differential electrocatalytic activation" as opposed to the generally accepted differential aeration based mechanism. Following this, techniques of inhibiting the localised corrosion of Mg in chloride containing electrolytes were investigated and it was found that only additions of sodium phosphate and sodium chromate showed any marked improvements in corrosion inhibition.

The concluding part of this thesis involved the investigation through Scanning vibrating electrode technique (SVET) of a technologically important alloy AZ91 and its localised corrosion behaviour. It was found following several hours of immersion in 5 w/v NaCl (aq) electrolyte that the corroded surface had become cathodically activated and it is proposed to be an enrichment in noble Al-Mn particles as anodic attack of the alpha Mg phase occurs.

Further SVET investigations with some rare earth cations showed that they in fact accelerated localised corrosion in comparison to the uninhibited electrolyte. As with C.P. Mg, chromate again proved to be an effected inhibitor by acting as a cathodic depolariser and it was suggested that the inhibition mechanism involves the reduction of chromate to Cr(iii) at cathodic sites, where elevated pH produces a solid Cr(iii) hydroxide film, which limits further electron transfer.

Declaration

This work has not been previously accepted in substance for any degree and is not being concurrently submitted in candidature for any degree.

Signed .... (candidate)

Date ...09/04/2013....

Statement 1

This thesis is the result of my own investigations, except where otherwise stated. Other sources are acknowledged by footnotes giving explicit references. A bibliography is appended.

Signed .... (candidate)

Date ...09/04/2013.......

Statement 2

I hereby give my consent for my thesis, if accepted, to be available for photocopying and for inter-library loan, and for the title and summary to be made available to outside organisations.

Signed .... (candidate)

Date ...09/04/2013....

ACKNOWLEDGEMENTS

I would like to acknowledge all the individuals that have supported and assisted in the completion of this PhD thesis.

I would particularly like to thank my supervisor, Dr. Geraint Williams for his continual support and expert guidance and help throughout the duration of my PhD and Dr. Amit Das for his generous advice. I would also like to thank Professor Neil McMurray for his insightful and invaluable comments at various stages in my work.

Finally, I would like to thank my family for all their help and support throughout my candidature.

CONTENTS

Abstract ii
Declarations and Statements iii
Acknowledgements iv
Contents v
List of Figures ix
List of Tables xv

1. Advanced Corrosion Mechanisms of Magnesium Alloys: Literature Review

1.1 Introduction 1

1.2 Basic Localised Corrosion Mechanisms 2
    1.2.1 Galvanic Corrosion 3
    1.2.2 Pitting Corrosion 4
    1.2.3 Crevice Corrosion 5
    1.2.4 Intergranular Corrosion (IGC) 6
    1.2.5 Stress Corrosion Cracking (SCC) 6
    1.2.6 Filiform Corrosion (FFC) 7
        1.2.6.1 General Characteristics of Filiform Corrosion 9
        1.2.6.2 Filiform Corrosion of Magnesium Alloys 10
        1.2.6.3 Initiation and Kinetics Parameters 13
        1.2.6.4 Propagation Mechanisms 14

1.3 Magnesium Alloys 15
    1.3.1 Corrosion Features of Specific Magnesium Alloys 16
        1.3.1.1 Elektron 21 16
        1.3.1.2 AZ31 18
        1.3.1.3 AZ91 22

1.4 Methods of Preventing Magnesium Corrosion 24
    1.4.1 Electrochemical Plating: Overview 25
    1.4.2 Conversion Coatings – Overview 28
        1.4.2.1 Chromate Conversion Coatings 28
        1.4.2.2 Phosphate-permanganate Conversion Coatings 29
    1.4.3 Hydride Coating 31
    1.4.4 Gas-phase Deposition Processes Overview 32
    1.4.5 Chemical Vapor Deposition 33
    1.4.6 Organic and Polymer Coatings 34
    1.4.7 Painting 37
    1.4.8 Powder Coating 39

1.5 Techniques for Characterizing Magnesium Corrosion 39
    1.5.1 Overview: From Polarization Curves to Scanning Electrochemical Techniques 39

1.5.2 Quantifying Corrosion 41
    1.5.2.1 Hydrogen (H2) Evolution 42
    1.5.2.2 Volumetric Mass Loss 42
    1.5.2.3 Tafel Extrapolation 43
1.5.3 Characterising Corrosion: 44
    1.5.3.1 EIS (Electrochemical Impedance Spectroscopy) 44
1.5.4 SVET (Scanning Vibrational Electrode Technique) 44
    1.5.4.1 Practical Application of SVET 49
1.5.5 SKPT (Scanning Kelvin Probe Technique) 50
    1.5.5.1 Practical Application of SKPT 52

1.6 Conclusions 53

1.7 References 54

2. Experimental Methodology 60

2.1. Introduction 60

2.2 Materials 60
    2.2.1 Metals 60
    2.2.2 Materials, Reagents and chemicals Used 60

2.3 Underfilm Corrosion Procedure 61

2.4 Time-lapse Photography 62

2.5 Hydrogen Evolution Technique 62

2.6 Open Circuit Potential Measurements (OCP) 64

2.7 Potentiodynamic Measurements 65

2.8 Scanning Vibrating Electrode Technique introduction 65
    2.8.1 SVET Apparatus 66
    2.8.2 S VET Sample Preparation 67
    2.8.3 SVET Calibration 68
    2.8.4 SVET Data Analysis 69

2.9 Scanning Kelvin Probe (SKP) Introduction 70
    2.9.1 SKP Apparatus 70
    2.9.2 SKP Operation 71
    2.9.3 SKP Calibration 72

2.10 References 73

3. Chloride-induced Filiform Corrosion of Organic Coated Magnesium 74

3.1 Introduction 74

3.2 Experimental Details 76

3.3 Results and Discussion 78
  3.3.1 FFC of Organic-coated Mg 78
  3.3.2 The Mechanism of Organic-coated Mg FFC 86
  3.3.3 FFC of Mg Under Immersion Conditions 91
  3.3.4 Mechanism of Mg FFC Under Immersion Conditions 97

3.4 Conclusions 100

3.5. References 101

4.Inhibition of Magnesium Localised Corrosion in Chloride Containing Electrolyte 103

4.1. Introduction 103

4.2. Experimental 106

4.3. Results and Discussion 108
  4.3.1 Localised Corrosion of Mg in Uninhibited 5% NaCl (aq) 108
  4.3.2 Screening of Potential Anionic Inhibitors 115
  4.3.3 Phosphate Inhibition of Mg Corrosion in NaCl Electrolyte 121

4.4. Conclusions 135

4.5. References 136

5. The localised corrosion of Mg alloy AZ31 in chloride containing electrolyte studied by a scanning vibrating electrode technique 139

5.1 Introduction 139

5.2 Experimental Details 141

5.3 Results and Discussion 143
  5.3.1 Localised Corrosion of AZ31 in 5% w/v NaCl (aq) 143
  5.3.2 Influence of pH on AZ31 Localised Corrosion in 5% w/v NaCl (aq) 162

5.4. Conclusions 171

5.5. References 172

6. Inhibition of the Localised Corrosion of Mg Alloy AZ31 in Chloride-containing Electrolyte 176

6.1. Introduction 176

6.2. Experimental Details 179

6.3. Results and Discussion 181
    6.3.1 Screening of Potential Corrosion Inhibitors 181
    6.3.2 Inhibition of AZ31 Localised Corrosion by Phosphate Anions 186
    6.3.3 Inhibition of AZ31 Localised Corrosion by Chromate Anions 194

6.4. Conclusions 204

6.5. References 205

7. Conclusions 211

7.1 Conclusions 211

LIST OF FIGURES

Figure 1.1: A schematic representation of the basic mechanism involved with filiform corrosion. 8

Figure 1.2: Solution treatment of as cast Elektron 21 performed at 525°C/8h in air, followed by immersion in water. 17

Figure 1.3: Calculation of corrosion rate due to weight loss of as cast Elektron 21 specimens (Samples were saturated with 3.5% NaCl for several days at room temperature). 18

Figure 1.4: Potentiodynamic polarisation curves obtained for the AZ31 Mg alloy V pre-treated for different times in $La(NO_3)^3$. All curves performed in 0.005 M NaCl. Scan rate 1mV/s. 20

Figure 1.5: Potentiodynamic polarisation curves obtained for the AZ31 Mg alloy pre-treated for different times in $Ce(NO_3)^{3.}$ All curves performed in 0.005 M NaCl. Scan rate 1mV/s. 21

Figure 1.6: Schematic representation of the current and potential distribution in solution above a localised anode set in a distributed cathode. 45

Figure 1.7: Shows the typical peaked shape when the probe is centred on the current source is clearly discernible 47

Figure 1.8: Schematic diagram illustrating the Kelvin probe (vibrating capacitor method) for measuring surface (Volta) potential. 53

Figure 2.1: A typical hydrogen evolution setup as used in this thesis. Apparatus include a $50cm^3$ Class B burette, glass funnel and measuring beaker. 64

Figure 2.2: Schematic illustration of the apparatus used for performing SVET measurements 66

Figure 2.3: Schematic diagram of specially designed two compartment SVET calibration cell 69

Figure 2.4: A typical SVET voltage and applied current density calibration plot 69

Figure 2.5: Schematic representation of the major components of the SKP apparatus 71

Figure 3.1: Photographic images of a PVB-coated, commercial purity Mg sample undergoing FFC attack in air at a constant relative humidity of 93%. Images were taken (a) 1h, (b) 24 h and (c) 48h following FFC initiation by applying aqueous HCl to a penetrative coating defect. 79

Figure 3.2: Interpolated grayscale maps showing SKP-derived E_{corr} distributions measured in air at 93% RH and 20°C over a PVB coated CP-Mg sample. Time key: (a) 12h, (b) 28h, (b) 40h and (d) 56h following initiation using a 1 μl quantity of 1 mol dm^{-3} HCl (aq). 81

Figure 3.3: Profiles of E_{corr} as a function of distance from the defect edge plotted centrally along the axis of filament propagation for a PVB coated CP-Mg sample. The time key is the same as for Figure 3.8. 82

Figure 3.4: Imaging SIMS greyscale maps, showing (a) secondary electron sample topography and (b) chloride ion distribution of a Mg surface affected by FFC, following removal of the PVB coating. The direction of FFC propagation is indicated by the dashed arrow. 83

Figure 3.5: Plot of mean filament length (L) vs time since FFC initiation on PVB coated CP-Mg measured in the (i) presence and (b) absence of air in 76% RH at 20° C after initiation of corrosion using a 1 µl quantity of aqueous 1 mol dm^{-3} Hcl. 84

Figure 3.6: Plot of mean filament length ($L - L_o$) vs time since FFC initiation on PVB coated CP-Mg measured at 20° C in air at a constant relative humidity of (i) 31%, (ii) 52% and (iii) 76% and (iv) 93%. L_o represents the initial coating disbondment length observed immediately after inoculating corrosion with a controlled quantity of 1 mol dm^{-3} HCl (aq). 85

Figure 3.7: Schematic representation of the mechanism of atmospheric FFC on magnesium in presence of an organic coating. 90

Figure 3.8: Photographic images of a commercial purity magnesium surface freely corroding in aerated 0.01 mol dm^{-3} NaCl (aq) at pH 6.5 taken at (a) 20 min, (b) 42 min and (c) 64 min following immersion. 93

Figure 3.9: Surface plots showing the distribution of normal current density j_z above a CP magnesium sample freely corroding in aerated 0.01 mol dm^{-3} NaCl (aq) at 20°C. Data were obtained from SVET scans carried out (a) 25, (b) 41, (c) 66, and (d) 100 min sample immersion. (e) shows the visual appearance of the same sample after 100 minutes immersion. 95

Figure 3.10: SVET-derived current density (j_z) profiles taken along a propagating cluster of filiform tracks on a freely corroding Mg surface immersed in 0.01 mol dm^{-3} NaCl (aq) at pH 6.5. Time key: (i) 17 min, (ii) 25 min and (iii) 33 min following immersion. 96

Figure 3.11: Schematic representation of the mechanism of magnesium FFC under immersion conditions, showing how the regions of the localised corrosion cell correspond with empirically derived SVET j_z versus distance profiles. 98

Figure 3.12: Secondary electron microscope image of an area of a CP-Mg surface affected by FFC after immersion in 0.01 mol dm^{-3} NaCl (aq). 98

Figure 3.13: Atomic force microscope 3-D topographic map of the tip of a corrosion filament obtained by immersion of a CP-Mg sample in 0.01 mol dm^{-3} NaCl (aq). 99

Figure 4.1: Surface plots showing the distribution of normal current density j_z above a CP magnesium sample freely corroding in aerated 5% w/v aqueous NaCl (aq) at pH 10 and 20°C. Data were obtained from SVET scans carried out immediately on immersion (a) and at (b) 12, (c) 24, and (d) 36 minutes after sample immersion. 112

Figure 4.2: Area-averaged anodic (i) and cathodic (ii) current density (J_t) values, calculated by numerical integration of SVET-derived current density distribution maps, plotted as a function of time for a CP-Mg sample immersed in aerated 5% w/w NaCl (aq) at pH10. 113

Figure 4.3: Comparison of the time-dependence of hydrogen evolution measured (i) volumetrically and (ii) via numerical integration of SVET-derived current density distributions for a CP-Mg sample freely corroding in 5% w/v aerated aqueous NaCl at pH 10 and 20°C. Plot (iii) shows the time-dependent variation of the area of exposed Mg comprising uncorroded, intact surface. 115

Figure 4.4: Area-averaged anodic current density versus time profiles obtained for magnesium immersed in aerated 5% w/v NaCl at pH 10 in the absence (i) and presence of 10^{-2} mol dm^{-3} additions of (ii) sodium fluoride, (iii) sodium phenyl phosphonate, (iv) sodium silicate, (v) sodium oxalate, (vi) sodium carbonate, (vii) sodium chromate and (viii) sodium phosphate. 117

Figure 4.5: Area-averaged anodic current density versus time profiles obtained for CP-Mg immersed in aerated 5% w/v NaCl (aq) at pH 10, containing (i) 10^{-4}, (ii) 10^{-3} and (iii) 10^{-2} mol dm^{-3} sodium chromate additions. Curve (iv) was obtained in the absence of inhibitor. 119

Figure 4.6: Area-averaged anodic current density versus time profiles obtained for CP-Mg immersed in aerated 5% w/v NaCl (aq) at pH 10, containing (i) 10^{-4}, (ii) 2×10^{-4}, (iii) 3×10^{-4}, (iv) 10^{-3} and (v) 10^{-2} mol dm^{-3} sodium phosphate additions. Curve (vi) was obtained in the absence of inhibitor. 120

Figure 4.7: SVET-derived current density surface maps of unpolarised commercial purity magnesium obtained 90 min following immersion in aerated 5% w/v NaCl (aq) at pH 10 containing a 10^{-3} mol dm^{-3} concentration of (a) sodium chromate and (b) sodium phosphate. 121

Figure 4.8: Area-averaged anodic current density versus time profiles obtained for magnesium immersed in aerated 5% w/v NaCl containing 10^{-3} mol dm^{-3} sodium phosphate at (i) pH 2.5, (ii) pH 4, (iii) pH 6, (iv) pH 8, (v) pH 10 and (vi) pH12. 122

Figure 4.9: Time-dependent hydrogen evolution, measured by a volumetric technique, observed for a CP-Mg sample freely corroding in aerated 5% w/v NaCl (aq) at pH 6, containing (ii) 10^{-4}, (iii) 10^{-3} and (iv) 10^{-2} mol dm^{-3} sodium phosphate additions. Curve (i) was obtained in the absence of inhibitor. 124

Figure 4.10: Photographic images showing the nature of the exposed Mg surface (a) when scanned by in-situ SVET in 5% w/v NaCl (aq) at pH 6 containing a 10^{-3} mol dm^{-3} addition of sodium phosphate and (b) after removal from the experimental electrolyte. (a) was taken 2h after immersion while (b) was recorded after 4h immersion time. 126

Figure 4.11: SVET-derived current density surface maps of unpolarised commercial purity magnesium obtained (a) 12 min and (b) 120 min following immersion in aerated 5% w/v NaCl (aq) at pH 6 containing a 10^{-3} mol dm^{-3} addition of sodium phosphate 127

Figure 4.12: Plot of E_{corr} with respect to time for CP-Mg samples immersed in aerated 5% NaCl (aq) at pH6.5 in the absence (i) and presence of (ii) 10^{-2} and (iii) 10^{-1} mol dm^{-3} sodium phosphate additions. 128

Figure 4.13: Schematic representation of the mechanism of magnesium corrosion inhibition by aqueous phosphate ions at neutral pH, showing (a) localisation of the early stages of corrosion, (b) phosphate speciation in the vicinity of the local cathode and (c) deposition of an insoluble film. 134

Figure 4.14: Schematic representation of a locally corroding magnesium surface in the presence of phosphate ions at elevated pH. 135

Figure 5.1: Surface plot showing the distribution of normal current density (j_z) above an AZ31 magnesium alloy sample immediately following immersion in aerated 5% w/v aqueous NaCl at pH 7, but prior to the breakdown of passivity. 144

Figure 5.2: The time-dependent variation of free corrosion potential (E_{corr}) observed upon immersion of AZ31 specimens in neutral, aerated aqueous electrolyte containing (i) 5%, (ii) 1% and (iii) 0.2% w/v concentrations of NaCl. 146

Figure 5.3: Photographic images showing the influence of immersion time of the appearance of a corroding AZ31 surface held in aerated 5% w/v NaCl (aq) electrolyte at pH 7 for (a) 10, (b) 30, (c) 60 and (d) 120 min. 147

Figure 5.4: Surface plots showing the distribution of normal current density (j_z) above a post-breakdown AZ31 alloy sample, freely corroding in aerated 5% w/v NaCl (aq) electrolyte at 20°C and pH 6.5. Data were obtained from SVET scans carried out (a) 12 min after immersion and at (b) 30 min, (c) 60 min, (d) 2h, (e) 4h and (f) 12h after sample immersion. 150

Figure 5.5: SVET-derived current density (j_z) profiles taken along the length of a dark corrosion track (indicated by the arrow in Fig 4b), observed on a freely corroding AZ31 surface immersed in 5% w/v NaCl (aq) at pH 6.5. Time key: (i) 12 min, (ii) 24 min and at 18 min intervals thereafter following immersion. 152

Figure 5.6: Area-averaged anodic (i) and cathodic (ii) current density values (J_a and J_c respectively), calculated by numerical integration of SVET-derived current density distribution maps, plotted as a function of immersion time. Plot (iii) shows the time-dependent variation of the area of exposed AZ31 comprising uncorroded, intact surface. Data was obtained from a 6 mm × 6 mm exposed sample area of AZ31 freely corroding in 5% w/v aerated aqueous NaCl at pH 7. 153

Figure 5.7: Time-dependent changes in an average value of normal cathodic current density (j_z) measured within a 1 mm^2 area of a freely corroding AZ31 specimen (curve i), where the vertical arrows indicate the points at which local anodes traverse the analysed area. The area over which average j_z values were calculated is again indicated by the arrow in Fig 5.4b. Curve (ii) shows a plot of J_a versus time determined over the same duration. 155

Figure 5.8: Comparison of the time-dependence of hydrogen evolution measured (i) volumetrically and (ii) via numerical integration of SVET-derived current density distributions for a AZ31 alloy sample freely corroding in 5% w/v aerated aqueous NaCl electrolyte at pH 7. 156

Figure 5.9: Anodic-going potentiodynamic polarisation curves obtained in aerated aqueous 5% w/v NaCl solution for an AZ31 alloy specimen. Curve i shows the initial data obtained for a sample immersed at OCP for 2 min, while curves ii and iii show data obtained after further 30 min and 3h holding times at OCP respectively. A sweep rate of 5 mV s^{-1} was employed in each case. 159

Figure 5.10: Schematic diagram showing proposed mechanism of AZ31 localised corrosion reconciled with a typical SVET-derived normal current density profile. 161

Figure 5.11: SVET-derived current density surface maps of unpolarised AZ31 magnesium alloy specimens obtained in aerated 5% w/v NaCl (aq) at various bulk pH values. The maps were determined at both 3h and 12h intervals following immersion at (a), (b) pH2; (c), (d) pH 12 and (e), (f) pH 13. 165

Figure 5.12: Area-averaged anodic (a) and cathodic (b) current density values (J_a and J_c respectively), calculated by numerical integration of SVET-derived current density distribution maps, plotted as a function of immersion time for a range of different electrolyte pH values. Data key; (i) pH 2, (ii) pH 4, (iii) pH 7, (iv) pH 10, (v) pH 12 and (vi) pH 13. The electrolyte used in each case was aerated 5% w/v NaCl (aq) at 20°C. 168

Figure 5.13: Time-dependent hydrogen evolution, measured by a volumetric technique, for AZ31 samples freely corroding in aerated 5% w/v NaCl (aq) at bulk electrolyte pH levels of (i) 2, (ii) 4, (iii) 7, (iv) 10, (v) 12 and (vi) 13. 169

Figure 5.14: Summary plot of total moles of hydrogen evolved over 6 h immersion versus bulk electrolyte pH for unpolarised AZ31 alloy specimens held in 5% w/v NaCl (aq), determined by (i) a volumetric technique and (ii) numerical integration of SVET derived cathodic j_z values. 170

Figure 6.1: Area-averaged anodic current density versus time profiles obtained for AZ31 alloy specimens immersed in aerated 5% (w/v) NaCl at pH 6.5 in the absence (i) and presence of 10^{-2} mol dm^{-3} additions of (ii) cerium (III) chloride, (iii) yttrium (III) chloride, (iv) sodium fluoride, (v) sodium chromate and (vi) sodium phosphate. 182

Figure 6.2: Surface plots showing the distribution of normal current density j_z above an AZ31 alloy surface after immersion for 1h in aerated 5% w/v aqueous NaCl (a) uninhibited, and in the same electrolyte with 10^{-2} mol dm^{-3} additions of (b) $CeCl_3$ and (c) YCl_3 at pH6.5 and 20°C. 184

Figure 6.3: Surface plots showing time-dependent changes in the normal current density j_z distribution for AZ31 alloy samples freely corroding in aerated 5% w/v NaCl (aq) electrolyte at 20°C and pH 6.5. (a) and (b) show data for an uninhibited sample at 60 and 240 min immersion times respectively. Plots (c) and (d) show the corresponding surface plots for AZ31 in the presence of a 10^{-3} mol dm^{-3} sodium phosphate addition, under the same conditions and at the same time intervals. Plots (e) and (f) are the corresponding surface maps obtained for a 10^{-2} mol dm^{-3} sodium phosphate addition. 188

Figure 6.4: Photographic images showing the nature of the exposed AZ31 surface taken 2h after immersion in (a) uninhibited 5% w/v NaCl (aq) at pH 6.5 and (b) in the same electrolyte containing a 10^{-2} mol dm^{-3} addition of sodium phosphate. 189

Figure 6.5: Area-averaged anodic current density versus time profiles obtained for AZ31 specimens immersed in (i) uninhibited, aerated 5% w/v NaCl (aq) at pH 6.5, and (ii), (iii) and (iv); the same electrolyte containing 10^{-4}, 10^{-3} and 10^{-2} mol dm^{-3} additions of sodium phosphate respectively. 190

Figure 6.6: Plot of E_{corr} with respect to time for AZ31 samples immersed in aerated 5% NaCl (aq) at pH 6.5 in the absence (i) and presence of (ii) 10^{-3}, (iii) 10^{-2} and (iii) 10^{-1} mol dm^{-3} sodium phosphate additions. 192

Figure 6.7: Photographic images showing the nature of the exposed AZ31 surface taken after removal from corrosive electrolyte following 2h immersion in uninhibited 5% w/v NaCl (aq) at pH 6.5 (a) and in the same electrolyte containing (b) 10^{-4}, (c) 10^{-3} and (d) 10^{-2} mol dm^{-3} additions of sodium chromate. 195

Figure 6.8: Plots of area-averaged anodic current density Ja_t versus immersion time for AZ31 samples freely corroding in 5% w/v aqueous NaCl at pH 6.5 in the absence (i) and presence of sodium chromate at concentrations of (ii) 10^{-2}, (iii) 10^{-3}, and (iv) 10^{-2} mol dm^{-3} 196

Figure 6.9: Surface plots showing the distribution of normal current density jz above an AZ31 alloy sample freely corroding in aerated 5% w/v aqueous NaCl containing a 10-2 mol dm-3 sodium chromate addition at pH6.5 and 20°C. Data were obtained from SVET scans carried out (a) immediately after immersion and at (b) 1h, (c) 4h and (d) 24 h after sample immersion 197

Figure 6.10: SVET-derived current density (jz) profile taken along the direction indicated by the arrow in Fig 6.9a, on a freely corroding AZ31 surface immersed in 5% w/v NaCl (aq) at pH 6 containing a 10^{-2} mol dm^{-3} sodium chromate immediately upon immersion. 199

Figure 6.11: E_{corr} versus time plots measured for AZ31 samples immersed in aerated 5% NaCl (aq) at pH 6.5 in the absence (i) and presence of (ii) 10^{-4}, (iii) 10^{-3} and (iii) 10^{-2} mol dm^{-3} sodium chromate additions. 200

Figure 6.12: Schematic showing proposed mechanism of localised corrosion inhibition on AZ31 in the presence of chromate anions. 202

Figure 6.13: The influence of varying inhibitor concentration on the localised corrosion of AZ31 in 5% w/v aqueous NaCl at pH 6.5, summarised by 4h total equivalent magnesium loss values calculated from SVET data for different concentration of (a) phosphate and (b) chromate inhibitor additions. 203

LIST OF TABLES

Table 1.1: Typical magnesium alloys systems and nominal compositions; ASM Handbook 15

Table 1.2: Table showing the chemical composition of Elektron 21 16

Table 1.3: Table showing the chemical composition of AZ31 Mg alloy 19

Table 1.4: Table showing the chemical composition of AZ91 Mg alloy. 22

Table 1.5: Table showing corrosion rates of AZ91 Mg alloy 23

Table 1.6: Table describes some of the most common pretreatment processes for metal coatings on magnesium. 27

Table 1.7 : Outline of the hydride coating formation process 31

Table 1.8: Organic finishing processes For Mg surfaces 35

Table 1.9: Surface treatments applied to AZ91 D Mg alloy prior to painting 38

Table 4.1: Literature values [29,30] of solubility products for magnesium salts formed with various anion types employed as inhibitors in this work. 116

Chapter 1

Advanced Corrosion Mechanisms of Magnesium Alloys: Literature Review

1.1 Introduction

Following Sir Humphrey Davy's electrolysis of the element in the early nineteenth century, magnesium has been consistently adopted for use in a variety of spheres; from its military-industrial applications throughout the first-world war to its inclusion in the manufacturing of automotive parts, magnesium is frequently part of cutting-edge technological research. This is unsurprising given that even the most basic features of the metal are highly desirable for a diversity of uses: magnesium is lighter than aluminium (being around two-thirds the density of the latter), it is strong, has an excellent strength-weight ratio, and is easily obtained through the electrolysis of brine, with China currently leading global magnesium production.

Despite its abundance of potentially profitable qualities, we must also be mindful of the significant limitations of the metal in its coherent form of pure magnesium. Indeed, it is well-documented that magnesium is not only brittle and highly reactive,(although this reactivity is cloaked to a certain extent by the process of passivation whereby a thin layer of oxide is deposited on the surface of the metal), but that it is also has extremely poor corrosion resistance. Of course, there are many instances in which these limitations have been harnessed for practical usage, for example the reactivity of magnesium led to its historical uses in fireworks, marine flares, and incendiary weaponry; however as I shall go on to discuss, for the present research these aspects of magnesium are considered as restrictions to a more effective use of the metal in engineering research. It is here that my own work finds its genesis, since even when employed in alloy form, scientific research has yet to overcome the aforementioned limitations of magnesium as an element.

Magnesium is most frequently alloyed with aluminium, resulting in alloys that are both light and durable, such as AZ31, and AZ91. As will be demonstrated in the range of materials discussed in the literature review to follow, research and development has thus far been unable to demonstrate any reliable method of negating the highly corrosive nature of the element. Consequently, alloys with higher percentages of magnesium such as A, B, and C, are still hampered by similar restrictions to pure magnesium itself. While throughout the course of this thesis my results will clearly indicate that some fundamental discrepancies in the current scientific understanding of the corrosion process in magnesium have certainly hindered more advanced anti-corrosion techniques, perhaps here it would be prudent to summarize the corrosion process itself, and how it has been characterised in the literature up to this point.

The purpose of a review of the existing literature on magnesium and its associated corrosion mechanisms is twofold: firstly, to highlight the considerable body of work that already exists in the field; and secondly, to situate my own research within that field as a means of filling the gap in current scholarship on magnesium alloys. This second purpose, the question of the research I have undertaken as part of this thesis, will be elucidated through the critical analysis contained within this chapter.

1.2 Basic Localised Corrosion Mechanisms

Before I begin to discuss the complexities of magnesium corrosion relevant here, I will first consider the basic mechanisms of corrosion that can affect magnesium alloys. As has been well-researched up to this point, there are several key types of localised magnesium corrosion. These include galvanic corrosion, pitting corrosion, crevice corrosion, intergranular corrosion (IGC), stress corrosion cracking (SCC) and filiform corrosion. Although it is work on filiform corrosion that comprises the bulk of the research related to this thesis, an understanding of other forms of corrosion is also important; these will be discussed in the sections that follow.

1.2.1 Galvanic Corrosion

Magnesium is the most active metal in the galvanic series[1].Galvanic corrosion has been a considerable hindrance to the use of magnesium in the automotive industry, particularly when employed in exterior vehicle parts[2]. It is well-known that magnesium alloys are extremely vulnerable to galvanic corrosion [Song and Atrens, 1999 [3]; Zeng et al., 2006 [4]]. This is often due to the alloying of magnesium with heavy metals and also to flux contamination, often a consequence of a badly-designed or badly-produced magnesium alloy. It usually manifests as heavy, localised corrosion of the metal surface adjacent to the cathode. The cathode can either be a metal that comes into contact with the magnesium alloy itself, or it can be caused by impurities within the alloy itself; thus it can be further separated into external and internal galvanic corrosion, respectively, but is observed macroscopically as general corrosion. This localised corrosion is most severe when the alloy comes into contact with metals with a low hydrogen overvoltage, such as iron, nickel, and copper, since these metals are very efficient cathodes for magnesium. Galvanic corrosion can therefore be reduced when metals with a high hydrogen overpotential and active corrosion potential come into contact with magnesium. Accordingly, the least damaging metals in terms of galvanic corrosion are usually cited as being aluminium, zinc, tin, and cadmium[3].

We can determine the theoretical rate of galvanic corrosion using the following equation:

$$i_g = (E_c - E_a) / (R_a + R_c + R_s + R_m) \qquad (1.1)$$

In the above equation, i_g is the galvanic current between the anode and the cathode. E_c and E_a are the open circuit potentials of the cathode and anode; R_c and R_a are the resistance of the cathode and anode, respectively; R_s is the resistance of the electrolyte solution between the cathode and the anode. R_m represents resistance through a metallic path from the surface of the anode to the surface of the cathode, but if the two electrode metals are in direct electrical contact, the value of R_m will be negligible. Therefore in theory, any factor that affects these parameters will have an effect on the rate of galvanic corrosion. In practice, however, given the complex interaction between the varying parameters, it can be difficult to estimate galvanic current or current density in reality [5].

The mechanism of galvanic corrosion is such that the high internal purity of the alloy does not necessarily ensure corrosion resistance if magnesium is combined with another metal, but corrosion resistance can be increased through the selection appropriate materials, better design of alloys, the use of coatings, and insulation of the alloy with other materials. The rate of galvanic corrosion is increased by electrochemical factors such as having a larger area ratio of cathode to anode, having an anode and a cathode in close proximity, high conductivity of the medium, low polarisability of the anode and cathode, and a large potential difference between the anode and the cathode.

1.2.2 Pitting Corrosion

Pitting corrosion is a localized form of corrosion where a particular area of the surface will undergo rapid attack while the rest remains largely unaffected , leading to small holes in the surface of the metal or alloy[6]. In fact, it is an extremely localised form of galvanic corrosion, whereby a small area becomes anodic through depassivation and a larger area becomes cathodic. While observable effects of this corrosion are often masked or seemingly insignificant, it damages microstructures within the metal to create weaknesses; some recent research has focussed on changing the microstructure as a means of protecting substrates against pitting corrosion. [7] It is a common form of corrosion in magnesium alloys when immersed in neutral or alkaline salt solutions, since as Song and Atrens note, magnesium is a naturally passive metal that upon exposure to chloride ions in a non-oxidising medium will undergo pitting corrosion at its free corrosion potential [3]. Pitting corrosion is accelerated by heavy metal contamination [8] In Mg-Al alloys, for instance, corrosion pits initiate along the $Mg_{17}Al_{12}$ network as a consequence of selective attack, resulting in the undercutting and falling out of grains [3].

1.2.3 Crevice Corrosion

Crevice corrosion is a form of corrosion similar to pitting corrosion that occurs, as its name suggests, in small spaces or "crevices" where moisture becomes trapped and causes active corrosion through a combination of two factors: the potential drop into the crevice itself and the chemical composition of the electrolyte therein. It is found at sites where there is one metal part and two connected environments, for example between a tube and a tube sheet. It was previously thought that crevice corrosion did not occur in magnesium alloys; however, as I shall go on to discuss in more detail below, filiform corrosion is now being considered as a specific type of crevice corrosion. Furthermore, Ghali et al., (2003) [9] speculate that crevice corrosion in magnesium alloys might be initiated by a hydrolysis reaction.

1.2.4 Intergranular Corrosion (IGC)

Intergranular corrosion is caused by the precipitation of the secondary phase, and manifests at grain boundaries. Since grain boundary phases in magnesium alloys are cathodic to the grain interior, for this reason some scientists argue that corrosion cannot penetrate inwards, and therefore that magnesium alloys are not susceptible to intergranular corrosion, for example as argued by Maker and Kruger, (1993)[10]. Ghali et al (2003) [9] also imply that IGC does not happen in magnesium alloys, although they do note that inter-crystalline corrosion, a form of IGC, often occurs in the initial stages of immersion. Therefore, while it is certain that IGC is not a major problem in the overall picture of magnesium alloy corrosion, research has demonstrated that we cannot say that it does not occur at all. In addition to Ghali et al. (2003), Valente (2001) reports IGC in WE43 magnesium alloy, a mechanism that was also apparent after immersion in an artificial sea-water solution, and that grain boundaries were the most vulnerable to IGC attack[11].

1.2.5 Stress Corrosion Cracking (SCC)

Stress Corrosion Cracking (SCC) refers to microscopic cracks that occur in certain alloys when in a corrosive environment; it is considered a dangerous form of corrosion since it is rarely observable or obvious until sudden failure. Winzer et al.(2005) note the three-way interaction that causes SCC: 1) Stress from mechanical loading; 2) a susceptible alloy; 3) an environment where there is an acceptable rate of corrosion [12]. SCC of magnesium alloys can occur in several corrosive environments, including moist air, high purity water, NaCl+K_2CrO_4 solution, NaBr, Na_2SO_4, NaCl, $NaNO_3$, Na_2CO_3, H_2SO_4, KF, Kcl, NaI, $MgCO_3$, NaOH, H_2SO_4, HNO_3, and hydrogen chloride solutions [13]. Increased rates of corrosion are also seen in aluminium alloys when exposed to chloride solutions, as well as air and distilled water [4].

Two distinct mechanisms are thought to be responsible for SCC in magnesium alloys; continuous crack propagation by anodic dissolution at the crack tip, or brittle fractures (discontinuous crack propagation) caused by hydrogen embrittlement (HE). These are referred to in the literature as the dissolution and embrittlement models. In addition to this, most researchers classify SCC into two types according to the fractures present in samples: transgranular SCC (TGSCC) and intergranular SCC (IGSCC). TGSCC is the most significant in magnesium and its alloys, and is associated with HE, while IGSCC is not a major cause of fracture in magnesium [3] [14]. According to Miller, experimental evidence for HE involvement in TGSCC includes:1) hydrogen evolution accompanying SCC initiation and propagation; 2) the appearance of similar fractures to SCC when sample is immersed in a cracking solution before the application of stress; 3) reversal of effects of pre-immersion in cracking solution when sample is exposed to vacuum annealing or to room-temperature air; 4) crack characteristics apparent when testing with gaseous hydrogen are identical to those produced in aqueous solution test; 5) SCC occurs at crack velocities that indicate only absorbed H could be present at the crack tip.

1.2.6 Filiform Corrosion (FFC)

Filiform corrosion is the corrosion mechanism most pertinent to this thesis, and therefore warrants significant treatment in this literature review. It was first described by Sharman in 1944, writing in the journal *Nature*, when he remarked the “growth of hair-like corrosion tracks known as ‘underfilm corrosion’” on the inside of old tobacco tin lids[14]. Fundamentally, filiform corrosion is localized corrosion that commonly occurs on magnesium alloys with an organic coating, as well as aluminium alloys and steel. The general diagram in Figure 1.1 illustrates the basic mechanism:

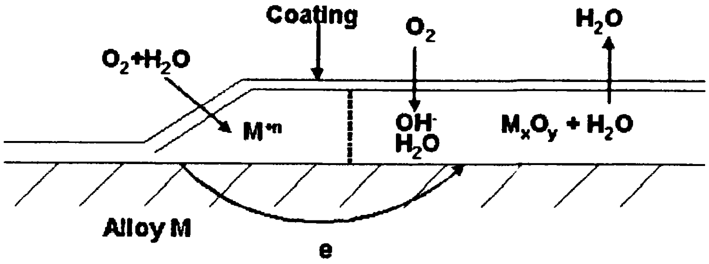

Figure 1.1: A schematic representation of the basic mechanism involved with filiform corrosion

It occurs at high humidity[15], and appears as worm-like structures, known as filaments, beneath the coating of the alloy, often causing this coating to bulge. From the above, we can describe the mechanism of filiform corrosion in simple terms: oxygen and water are able to permeate the coating of an alloy, and where the oxygen concentration becomes highest at the tail region, the area becomes cathodic. The head therefore becomes the anode, since this is where oxygen is depleted. The impetus behind the corrosion mechanism, then, comes from the potential difference between these two areas.

Though it is largely considered to be a superficial form of corrosion that does not damage the internal structure of the metal alloy, it is still true that research on filiform corrosion is nonetheless in high demand. Given the application of many metal alloys in the automotive and aerospace industries, many manufacturers seek to constantly improve the external appearance of products that contain these alloys in response to market demand . However, filiform corrosion is not merely a superficial concern, since FFC has also long been known to facilitate stress corrosion cracking around rivet heads leading to catastrophic results in aeronautic applications[16].

1.2.6.1 General Characteristics of Filiform Corrosion

As I have already mentioned, FFC can occur on aluminium and iron alloys as well as magnesium alloys, and most research indicates that the fundamental mechanisms of filiform corrosion occur under similar environments, as well as sharing some electrochemical processes that I shall briefly discuss here; however, I will then go on to consider the specific mechanisms of FFC in relation to magnesium alloys, as is the main remit of this thesis.

Generally, for FFC to occur on an alloy, one or more of the following conditions are present, according to [19][17][18]:

a) Initiates at points in the coating where weaknesses or defects can be identified.

b) Can only occur between a relative humidity of 30 – 95%.

c) Propagation of FFC requires oxygen

d) Initiation requires aggressive anions.

e) Anions of the inoculating salt (most frequently a chloride salt) are conserved in the filiform head; cations are not.

f) Front edge of the filiform head is the most anodically active area, and usually contains a low pH solution.

g) Size and speed of filament cells are not contingent on the physical properties of the alloy coating.

h) Filament motion is stable, and tracks will propagate in the rolling direction.

i) Generally, tracks neither cross nor break the surface coating, but there are isolated examples of this in the literature.

The filament itself moves across the surface of a metal alloy by means of an "active" head and a "passive" tail, where the head contains an electrolyte and the tail contains porous corrosive products. In their analysis of mass transfer in FFC, Ruggieri and Beck confirm through experimental evidence that the transfer of oxygen and water into the corrosion site does indeed occur via the porous tail[19]. This preferred mechanism for FFC has been consistently noted by other scholars, from earlier to more current research. Although some initial scholarly research did suggest that FFC might caused by diffusion through the coating products, this theoretical view is now considered defunct, since calculations indicate that oxygen transport through the coating would be ten times slower than through the porous tail marking a coating defect [19] Since oxygen is supplied through the tail in a unidirectional manner, a differential aeration cell is established at the filament head, whereby the deaerated front of the head forms the anode and the aerated back of the head forms the cathode. It has therefore been established in the literature that as a consequence of this differential aeration cell, the oxygen reduction occurs at the back of the head in a cathodic reaction, causing metal dissolution at the front of the head in an anodic reaction. But how does the literature characterise this corrosion mechanism in the specific case of magnesium alloys?

1.2.6.2 Filiform Corrosion of Magnesium Alloys

Although filiform corrosion is not observed on bare pure magnesium, the scientific literature on corrosion suggests that aluminium and magnesium alloy filiform corrosion basically function according to the same corrosive principles. While the bulk of this thesis will demonstrate that this notion is in fact flawed, since magnesium alloys do not conform to the same corrosion patterns as those observed in aluminium alloys,

Williams et al. have shown that the rate of FFC advance is in fact insensitive to the presence